

RESEARCH

Open Access



Preparation and characterization of polymyxin B- and histidine-coupled magnetic nanoparticles for purification of biologics from acquired endotoxin contamination

Al-Shaimaa M. Salah^{1*} , Lamiaa A. Hassan¹, Faten Fathallaa¹, Medhat A. Al-Ghobashy^{2,3} and Marianne Nebsen²

Abstract

Background: Endotoxin is a major process-related impurity that can act as a strong immunostimulant leading to fever and hypotensive shock. Thus, the US FDA and international quality standards strictly direct the biologics manufacturers to control the endotoxin contamination during the purification process. In this work, a developed method for biologics purification from acquired endotoxin contamination is introduced. This is accomplished by the preparation of dextran-coated magnetic nanoparticles using a facile rapid co-precipitation method.

Results: The resulting magnetic nanoparticles (MNPs) are characterized by dynamic light scattering, transmission electron microscope, Fourier transform infrared spectroscopy, X-ray diffraction, and vibrating sample magnetometry. The dextran-coated magnetic nanoparticles are further coupled to either polymyxin B or histidine to provide a positively charged ligand which enhances the affinity to the negatively charged endotoxin. Both ligands-coupled MNPs are tested for purification efficiency using the chromogenic kinetic assay. The method conditions are optimized using a two-level factorial design to achieve best purification conditions of the contaminated biologics and indicated endotoxin removal percentage 85.12% and maximum adsorption capacity of 38.5 mg/g, for histidine-coupled MNPs.

Conclusions: This developed method is introduced to serve biologics manufacturers to improve their manufacturing processes through providing a simple purifying tool for biologics from acquired endotoxin contamination.

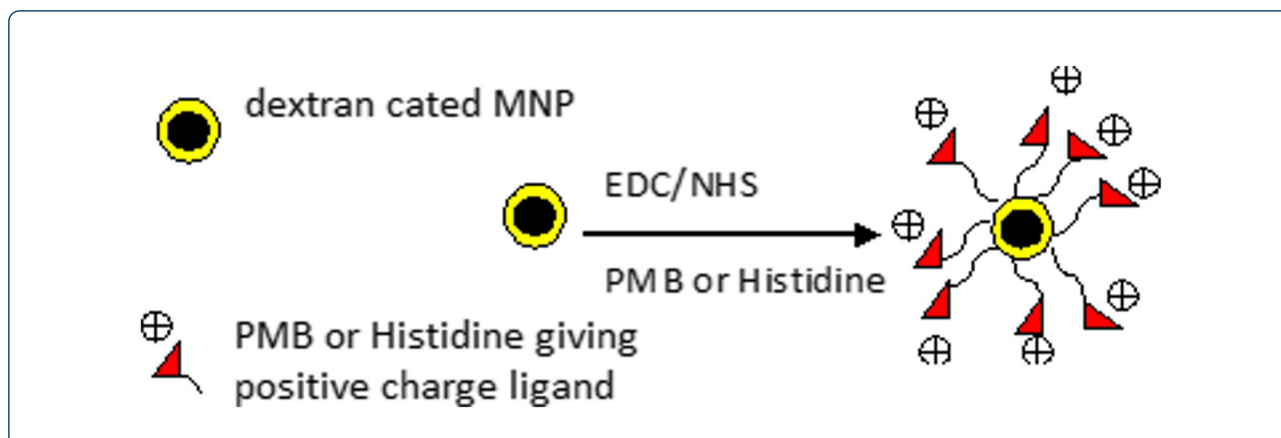
Keywords: Endotoxin, Polymyxin B, Histidine, Magnetic nanoparticles, Biologics, Purification

Graphical Abstract

*Correspondence: dr_alshaimaa13_12@yahoo.com

¹ Egyptian Drug Authority, Cairo, Egypt

Full list of author information is available at the end of the article



1 Background

Endotoxins are one of the most challenging impurities requiring separation in biologics purification processes. They arise from the outer cell membrane of Gram-negative bacteria that are widely used in biologics manufacturing [1, 2]. The Gram-negative bacteria could be used in biological manufacturing processes as a raw material as, for example, in the interferon manufacturing process, the *E. coli* works as a host cell which remnant displays a source of endotoxin [3]; also, there are types of vaccines, for example, the meningococcal polysaccharide vaccine that depends on the extraction of the immunogenic part from the cell wall of the gram-negative bacteria *N. meningitidis* which remnant also introduces endotoxin as contaminant [4]. Endotoxins are lipopolysaccharides made up of three different parts: the O-specific chain, the core region, and the lipid A. The lipid A region is ordinarily composed of two glucosamine units with attached fatty acids [5]. The phosphorylated glucosamines give endotoxins a net negative charge [6]. Lipid A is hence an amphiphilic glycolipid that has the capacity to acquire different physical structures under different temperature or pH conditions. It represents the single region of endotoxin recognized by the immune system [5, 7]. According to the US FDA, the maximum acceptable endotoxin levels in intravenous drugs or biologics were 5.0 endotoxin units per kilogram of body weight that can be administered to a patient per hour [8]. This regulation obliges pharmaceutical/biologics companies to follow and control their intravenously administered drugs for bacterial endotoxin/pyrogen contaminations [9]. As long as endotoxin contamination should be controlled and regularly monitored along the manufacturing process, most users rely on the conventional endotoxin detection methods such as the rabbit pyrogen test (RPT) [5] and the limulus amoebocyte lysate assay (LAL) for regular monitoring. Pharmaceutical/biological manufacturers tend to use more sensitive and accurate endotoxin

detection methods and shift away from using living test subjects, that's why rabbit pyrogen test is only applied now in the early development stages of pharmaceutical/biological products beyond which LAL assay is favored [8]. Different methods of the LAL assay are available: the gel-clot assay, the chromogenic substrate method, and the turbidimetric method [10]. An advancement of the LAL detection method was applied with the discovery of zymogen factor C, which is used in the chromogenic method with more accuracy and sensitivity (0.005 EU/mL) than the older gel-clot assay (0.03 EU/mL) [5, 11]. Furthermore, chromogenic substrates can be adapted to assess endotoxin adherent to a biomaterial, resulting in the determination of endotoxin contamination in terms of equivalent endotoxin units/mL (using the calibration curve from standard solutions) [11]. The up-to-date research tends to transform endotoxin detection from conventional methods to newly developed methods such as biosensors, recombinant factor C assay, monocyte activation test, and surface plasmon resonance, to overcome the problems associated with the LAL-based method as false-negative and false-positive results [12]. Moreover, numerous analytical techniques have been adopted for the purification of biologics from acquired endotoxin, including ultrafiltration, size exclusion chromatography, affinity chromatography, and adsorption on anion exchange chromatography [9, 13]. However, ultrafiltration is suitable to separate endotoxins only from small target therapeutic drug molecules, which is not generally applicable for biologics [8]. Size exclusion chromatography has a limited capacity and selectivity. Affinity chromatography consumes high time and has a low yield [14]. Moreover, anion exchange chromatography owes expensive and complex procedures [15]. Various affinity ligands showed good specificity for endotoxin binding, such as polymyxin B (PMB) and histidine (HIS) [16, 17]. Both PMB and HIS have potential removal of endotoxin from various proteins with high recovery percentage [1].

Recently, iron oxide nanoparticles have attracted much consideration due to their unique characteristics, such as superparamagnetism, higher surface area, surface-to-volume ratio, and simple separation methodology [18, 19]. The stabilization of the iron oxide particles is important to obtain magnetic colloidal ferrofluids that are stable against aggregation in both a biological medium and a magnetic field. Dextran has been used often as a polymer coating for MNPs mainly because of its biocompatibility [19], moreover acting as a surfactant creating steric repulsive forces enhancing particle stabilization [20].

The aim of the current study is to synthesize, characterize, and evaluate dextran-coated MNPs coupled to PMB and HIS. The prepared MNPs are characterized by dynamic light scattering (DLS), transmission electron microscope (TEM), Fourier transform infrared spectroscopy (FTIR), X-ray diffraction (XRD), and vibrating sample magnetometry (VSM). Furthermore, the prepared MNPs are evaluated for the endotoxin removal ability by the chromogenic kinetic assay and their adsorptive kinetics and adsorption isotherm were studied as well.

2 Methods

2.1 Chemicals and reagents

Endosafe® LAL cartridges and Endosafe Water for LAL (WFL) were purchased from Charles River (USA). LPS derived from *E. coli* serotype (O55:B5) was purchased from Sigma (USA). All used chemicals such as ferrous chloride tetrahydrate ($\text{FeCl}_2 \cdot 4\text{H}_2\text{O}$), ferric chloride hexahydrate ($\text{FeCl}_3 \cdot 6\text{H}_2\text{O}$), dextran 40-T, polymyxin B sulfate, L-histidine, 1-(3-dimethylaminopropyl)-3-ethylcarbodiimide hydrochloride (EDC), and sulfo-N-hydroxysulfosuccinimide (S-NHS) were of analytical grade and purchased from Sigma (USA).

2.2 Preparation and optimization of dextran-coated MNPs

Dextran-coated MNPs (DC-MNPs) were prepared via employing chemical co-precipitation methods [21–28]. This is accomplished through dissolving 0.64 g $\text{FeCl}_2 \cdot 4\text{H}_2\text{O}$ and 1.51 g $\text{FeCl}_3 \cdot 6\text{H}_2\text{O}$ (molarity 1:2) in 10 mL of sonicated water for LAL (WFL) and then mixed with 10 mL of 50% w/v dextran solution. The pH was adjusted to 9.0 by adding 28% ammonia solution during shaking; the produced blackish-brown mixture was incubated at 85 °C for 15 min with shaking. After incubation, the solution was centrifuged for three cycles at 7000 rpm, each cycle 5 min except the last one 20 min, and the supernatant containing the MNPs was preserved. The prepared MNPs were dried at 90 °C for 6 h. The preparation conditions were optimized through the application of a two-level fractional factorial design with one center point using Minitab 2010. The optimized factors were the molarity of iron salts, the weight ratio of dextran, pH of

preparation, concentration of ammonia solution, heating temperature, and time of heating. Dynamic light scattering (DLS) was used in estimating the average hydrodynamic diameter of the coupled MNPs and their size distribution in terms of polydispersity index (PDI).

Coupling of the ligand, either PMB or HIS, was accomplished according to the modified protocol [29], through dispersing the MNPs powder in the activation phosphate buffer at pH 6.0. Then, 50 mg/ml EDC solution and 50 mg/ml S-NHS solution were added to the activated MNPs. After that, MNPs were sonicated, kept in the dark for 20 min, and centrifuged at 14,000 rpm for 6 min. The precipitate was redispersed in phosphate-buffered saline (PBS) solution, mixed well, and sonicated. The ligand solution of equal volume was added to the MNPs solution and kept in the dark for 2 h with mild shaking. The coupled MNPs were separated by centrifugation, then washed several times by WFL, and kept in PBS solution.

2.3 Characterization of the prepared MNPs

The MNPs were characterized using TEM, VSM, XRD, and DLS, while the effective coupling of the ligand was confirmed through FTIR.

2.3.1 Transmission electron microscope (TEM)

TEM images of MNPs were obtained using JEOL 2100 transmission electron microscope. A field emission source was operated at 160 kV. Nanoparticles were deposited on a copper-grid-supported holey carbon foil and left to dry in air and then examined.

2.3.2 X-ray diffraction (XRD)

XRD measurements were performed in a Rigaku model Geigerflex apparatus using $\text{CuK}\alpha$ radiation from 10 to 70° (2θ) at a scan rate of 4° min^{-1} .

2.3.3 Magnetization measurements

The magnetization curves of MNPs were attained at room temperature with a Princeton EG and G Applied Research vibrating sample magnetometer (VSM).

2.3.4 Dynamic light scattering (DLS)

DLS was performed to determine the hydrodynamic size, size distribution, and zeta potential of MNPs. The measurements were performed on a Zetasizer Nano-ZS ZEN 3600 (Malvern Instruments Ltd.). The analysis of Brownian motion offers a powerful tool to measure the diameter of the prepared MNPs and diffusion coefficient through the autocorrelation function. For potential measurement, a combination of laser Doppler velocimetry and phase analysis light scattering was used in measuring particle electrophoretic mobility. All measurements were carried

out under equilibrium conditions. Measured samples were diluted in WFI to neutral pH at room temperature.

2.3.5 Fourier transform infrared spectroscopy (FTIR)

To study the effectiveness of coating and coupling of the MNPs, FTIR analysis of the samples was performed by compacting the samples to form a tablet using KBr as the matrix and the samples were analyzed in the transmission mode. The spectra were detected over a range of 4000–500 cm^{-1} and recorded by JASCO 1600, PerkinElmer Spectrum GX, and Bruker mobile IR Spectrometer.

2.4 Adsorption of control bacterial endotoxin on ligand-coupled MNPs and optimization of the experimental design

The ligand-coupled MNPs were incubated with the control bacterial endotoxin (CBE) solution after mixing and sonication. The solution was centrifuged at 14,000 rpm for 6 min, and the supernatant was kept. The bacterial endotoxin (BE) content of the CBE was determined by chromogenic kinetic assay using a multi-cartridge system (MCS), which provides endotoxin test results for up to five samples in about 15 min. The efficiency of purification removal of endotoxin was calculated using the following equation:

$$E = ((C_0 - C) \div C_0) \times 100$$

where E is the removal efficiency, C_0 and C are the concentrations of endotoxin in the initial solution and in the supernatant after adsorption, respectively.

The adsorption conditions were optimized through the application of a two-level fractional factorial design with one center point using Minitab ver. 16.1.1, 2010.

The optimized factors were ligand type, ligand concentration, BE concentration, pH range of incubation, the temperature of incubation, and time of incubation.

2.5 Chromogenic kinetic assay

The control bacterial endotoxin (CBE) was prepared by reconstitution of the LPS with water for LAL (WFL) to have a concentration of 10×10^6 EU/mL of CBE which was diluted as required by WFL. The tested samples were diluted by WFL as required. Kinetic chromogenic LAL reagent is used in a pre-calibrated, single-use, Endosafe® LAL test cartridge; the tested solution was added to each channel of the test cartridge of the Endosafe multi-cartridge system (MCS, Charles River) according to the instructions of the device manual. The device's internal pump moves the sample along the channels' reagent stations for mixing and then into the optical cells of the cartridge to be read kinetically. Measurements of the endotoxin content of the prepared CBE and samples were done through the chromogenic kinetic method using

multi-cartridge system [10]. The endotoxin level of each sample was measured before and after exposure to the adsorption experiment.

2.6 Kinetics of adsorption

A kinetic study was performed by incubation of 0.1 mg of CBE with 0.05 g of both types of ligand-coupled MNPs for different time intervals (5–105) min. After each time interval, the concentration of residual endotoxin in solution was determined and the amount of endotoxin adsorbed at each time interval (q_t , mg g^{-1}) was plotted against time (t , min) for kinetic study. Four kinetic models were explored including pseudo-first-order, pseudo-second-order, Elovich, and intraparticle diffusion model to investigate the adsorption kinetics and adsorption mechanism in correlation with the experimental parameters [30, 31].

The linearized kinetics equations were presented as follows:

Pseudo-first-order kinetics or Lagergren model

$$\log(Q_e - Q_t) = \log Q_e - \frac{k_1}{2.303} t$$

Pseudo-second-order kinetics or Ho and McKay model

$$\frac{t}{Q_t} = \frac{1}{K_2 \cdot Q_e^2} + \frac{1}{Q_e} t$$

Elovich kinetic equation

$$Q_t = \frac{1}{\beta} \ln(\alpha\beta) + \frac{1}{\beta} \ln t$$

Intraparticle diffusion kinetic model

$$q_t = k_p \cdot t^{1/2} + C$$

where Q_e and Q_t (mg/g) denote the endotoxin adsorption capacity at equilibrium and at time t (min), respectively; K_1 is the rate constant of pseudo-first-order adsorption (min^{-1}); K_2 is the rate constant of pseudo-second-order model adsorption ($\text{mg} \cdot (\text{mg min})^{-1}$); β is the Elovich constant related to the surface coverage (g mg^{-1}); and K_p is an intraparticle diffusion rate constant ($\text{mg} \cdot (\text{l/mg} \cdot \text{min}^{-0.5})$).

The equilibrium capacity of adsorption (Q_e expt.) was calculated using the mass balance equation $Q_T = (C_0 - C_t) \times (V/m)$, where C_0 and C_t (mg/mL) are the initial and final endotoxin concentrations, respectively, V (mL) is the volume of the solution, and m (g) is the mass of adsorbent. When t is equal to the equilibrium time, that is, $C_t = C_e$,

$Q_t = Q_e$, then Q_e can be calculated using the same equation as given above [32].

2.7 Adsorption isotherm

Equilibrium isotherm studies were carried out with different initial concentrations of adsorbent (histidine and PMB) 0.05, 0.28, and 0.5 mg at 25 °C and pH 6.5 for initial CBE concentration of 0.1 mg/ml and incubation time 30 min.

The equilibrium adsorption data were analyzed using two different models:

Langmuir, with linearized equation:

$$q_c = \frac{Q_0 b C_e}{(1 + b C_e)}$$

Freundlich, with linearized equation:

$$\ln q_e - \ln K_f + \left(\frac{1}{n}\right) \ln C_e$$

where C_e is the equilibrium concentration of endotoxin in the solution (mg/ml), q_e is the amount of endotoxin adsorbed per unit mass of adsorbent (mg/g), b the Langmuir equilibrium constant (mL/mg) and related to energy of adsorption. Q_0 signifies the maximum adsorption capacity (mg/g), which depends on the number of adsorption sites; K_f ($\text{mg}^{1-1/n} \text{mL}^{1/n} \text{g}^{-1}$) and $1/n$ are Freundlich constants depending on the temperature and the given adsorbent adsorbate couple. n is related to

the adsorption energy distribution, and K_f indicates the adsorption capacity [32, 33].

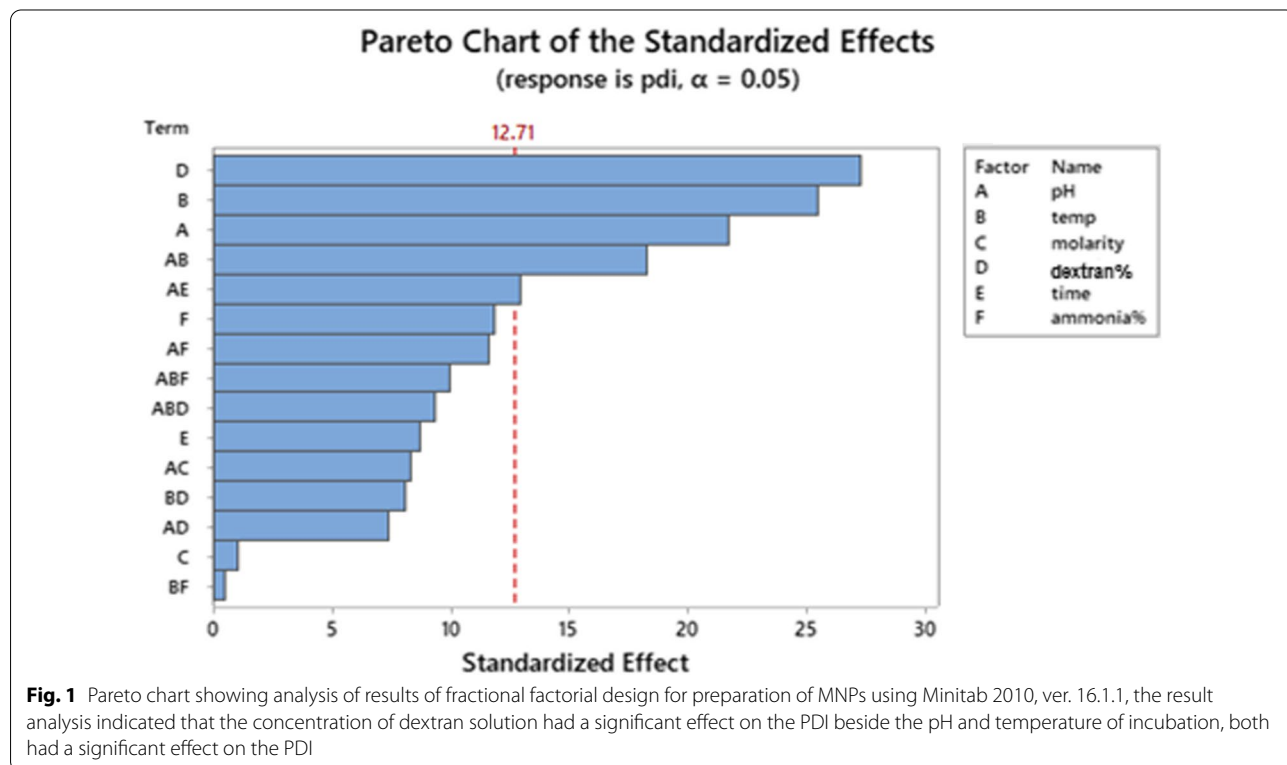
2.8 Applications to incurred samples

The optimized experiment was applied for the purification of biological finished products of pegylated interferon and meningococcal polysaccharide spiked with 500,000 EU/mL CBE, and the residual endotoxin was measured by chromogenic kinetic assay and the %removal of endotoxin was calculated.

3 Results

3.1 Preparation and optimization of dextran-coated MNPs

Dextran-coated MNPs (DC-MNPs) were successfully synthesized by the previously described co-precipitation method as a result of the factorial design analysis. The preparation method was optimized by studying the effect of different factors on the size and PDI of the MNPs using DLS as an assessment guiding tool. Two levels of each factor were chosen beside one center point to determine the optimum conditions for preparation. Analysis of the fractional factorial design results was conducted at 95% confidence level ($P < 0.05$) using the size and PDI as the response factors. A Pareto diagram was used to establish conclusions on the relative significance of the studied factors as well as the interactions between them (Fig. 1). Upon analysis of the experimental data, as shown



in Table 1, it was found that the concentration of dextran solution had a significant effect on the particle size distribution (PDI) and solid content of the prepared MNPs. The pH and temperature of incubation had a significant effect on the PDI (Fig. 1). The selected design experiment conditions as shown in run order no. 14 in Table 1 were employed to introduce one of the smallest particle sizes (59.04 nm) with very acceptable PDI (0.275), and this pilot experimental design was used to implement the rest of the experiment.

3.2 Characterization of the prepared MNPs

3.2.1 Transmission electron microscope (TEM)

The developed dextran-coated MNPs, when scanned through TEM, appeared to be nearly spherical in shape, arranged in lattice form as shown in Figs. 2, 3, and 4 distributed within the dextran matrix with average size 2–10 nm and aggregated in a cluster form with an average size range 50–100 nm.

3.2.2 X-ray diffraction (XRD)

The crystalline nature for dextran-coated MNPs was investigated by XRD analysis, and the resulted peaks are presented in Fig. 5. There were six diffraction peaks (220), (311), (400), (422), (511), and (440). The FWHM (full width at half maximum) of the major diffraction peak (311) was used to calculate the average particle size of the prepared MNPs through the use of Scherrer

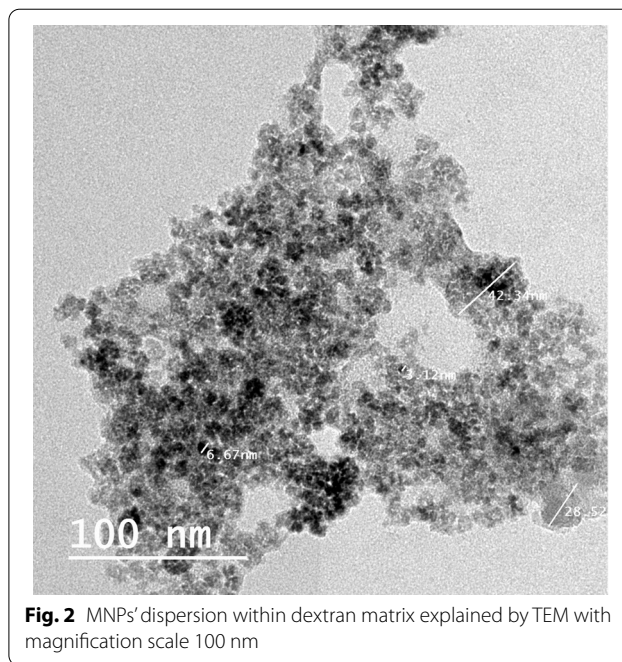


Fig. 2 MNPs’ dispersion within dextran matrix explained by TEM with magnification scale 100 nm

formula [34] as follows: $D = 0.9\lambda / \beta \cos \theta$ where λ is the wavelength of X-ray (0.15405 nm), β is FWHM, θ is the diffraction angle, and “D” is the particle diameter.

Table 1 Fractional factorial design for optimization of preparation of MNPs with results showing the selected experiment (run order 14)

Run order	pH	Temp	Molarity of iron salts	Dextran%	Time	Ammonia%	z-average	Pdl	pk1 area intensity%
1	11	60	2:1	20	15	28	51.26	0.467	91.3
2	9	60	2:1	20	60	28	89.71	0.302	93.8
3	11	85	2:1	50	60	28	54.16	0.376	52.5
4	11	85	1:1	20	15	28	82.66	0.643	83.1
5	11	85	1:1	50	15	7.5	104.8	0.371	91.7
6	10	72.5	1:1	35	37.5	17.75	117.6	0.249	100
7	11	60	1:1	50	60	28	70.22	0.27	97.1
8	11	60	2:1	50	15	7.5	92.38	0.26	100
9	10	72.5	2:1	35	37.5	17.75	81.87	0.264	100
10	9	85	2:1	20	15	7.5	89.53	0.308	100
11	9	60	1:1	50	15	28	104	0.229	99
12	9	60	1:1	20	15	7.5	90.15	0.358	85.1
13	9	85	1:1	20	60	28	99.7	0.401	98.8
14	9	85	2:1	50	15	28	59.04	0.275	98.2
15	11	85	2:1	20	60	7.5	493.4	0.533	58.7
16	11	60	1:1	20	60	7.5	115	0.205	100
17	9	85	1:1	50	60	7.5	96.06	0.28	98.8
18	9	60	2:1	50	60	7.5	65.74	0.257	95

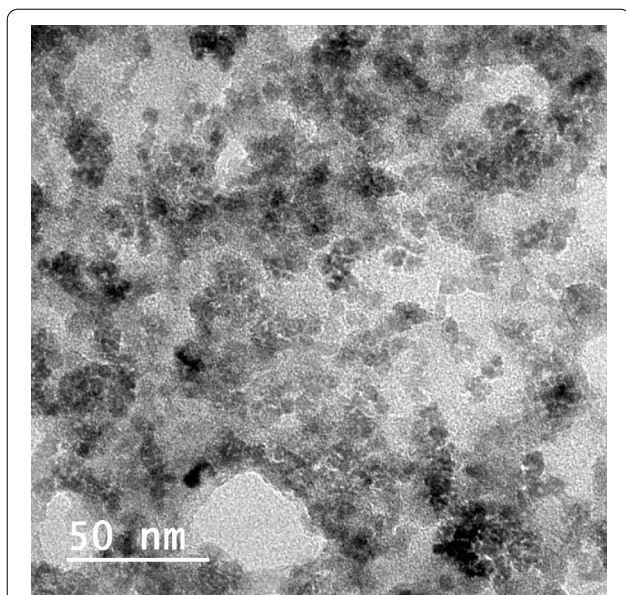


Fig. 3 MNPs' dispersion within dextran matrix explained by TEM with magnification scale 50 nm

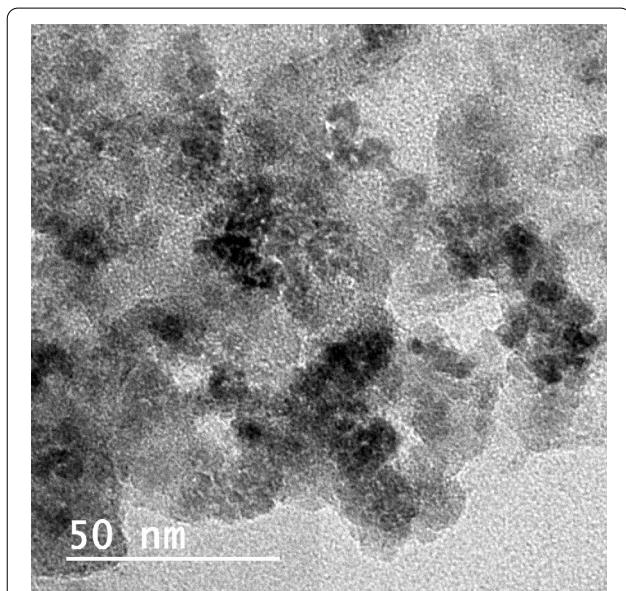


Fig. 4 MNPs' dispersion within dextran matrix explained by TEM with magnification scale 200 nm

3.2.3 Magnetization measurements

The magnetic properties of the developed MNPs were investigated using VSM, and the magnetic behavior of the MNPs was studied by recording the magnetization (M) against the applied magnetic field (G) at room temperature. The analyzed sample revealed masked superparamagnetism as shown in (Additional file 1: Fig. S-1).

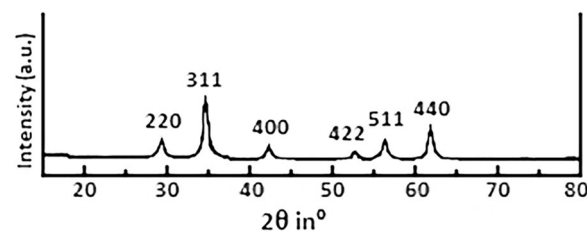


Fig. 5 X-ray diffraction chart presenting the magnetite characteristic peaks

The saturation magnetization (M_s) was found to be $1.2106E^{-3} \text{ emu g}^{-1}$.

3.2.4 Dynamic light scattering (DLS)

3.2.4.1 Zeta potential The surface charge of MNPs samples was studied using a Zetasizer Nano ZS, at neutral pH. The MNPs obtained a zeta potential value of -12.4 ± 2.5 .

3.2.4.2 Particle size distribution The size of MNPs after modification with dextran shell was studied by DLS using a Zetasizer Nano ZS; the size of the nanoparticles was about $69.55 \pm 2.97 \text{ nm}$. Figure 6 reveals only one peak with a good PDI value of 0.283 ± 0.0056 .

3.2.5 Fourier transform infrared spectroscopy (FTIR)

Fourier transform infrared spectrometry was introduced to investigate the effective coupling of the ligand to the MNPs. In the FTIR spectrum of dextran-coated MNPs (Additional file 1: Fig. S-2), the peak at 3283.5 cm^{-1} represented hydroxyl groups [32], while the intense peaks at 1636.2 and 1021.12 cm^{-1} were due to the stretching vibration of the (C–O) bond and the band at 2923.3 cm^{-1} was attributed to the bending vibration of CH_2 groups [35]. The band at around 620 cm^{-1} appeared due to the stretching vibration of Fe–O bond [32]. In the FTIR spectrum of pure PMB, the peak at 3408.8 cm^{-1} represented the amino groups and the specific peak at 1635.8 cm^{-1} was attributed to the amide functional group [36].

By comparing FTIR spectra of pure PMB and DC-MNPs to the spectrum of DC-MNP coupled to PMB, the relevant peaks of dextran and Fe–O bonds appeared at the same positions, without remarkable shifting. In addition, the peaks of PMB appeared at the same positions corresponding to the amino and amide groups and no significant shifts were noticed between free PMB and the trapped by MNPs [36].

For pure HIS (Additional file 1: Fig. S-3), the characteristic amino group stretching vibration was noticed at 3330 cm^{-1} , while asymmetric and symmetric stretching vibrations of the carboxylate group were observed

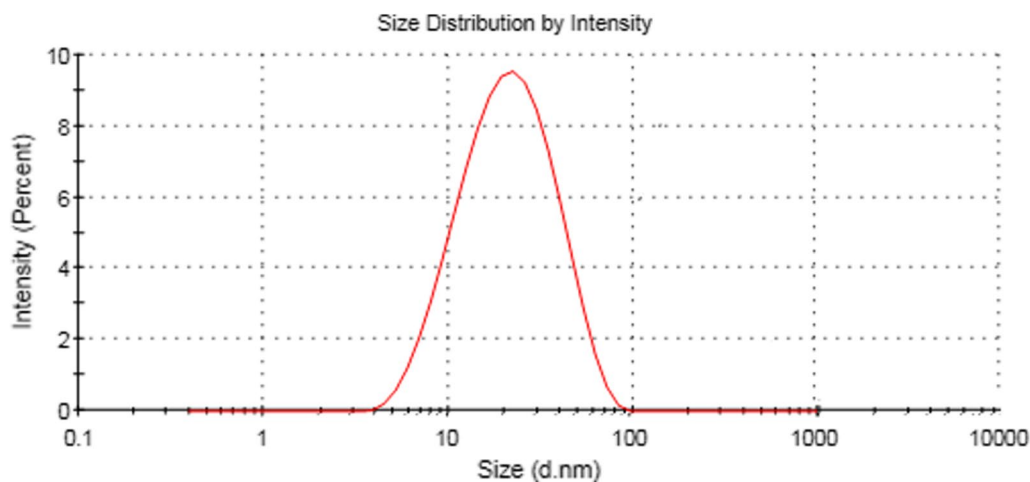


Fig. 6 Particle size distribution of DC-MNPs by DLS showing a particle size of 69.55 ± 2.97 nm with very good size distribution introduced in the PDI value of 0.283 ± 0.0056

at 1635 and 1411 cm^{-1} , respectively. By comparing the FTIR spectrum of pure HIS to the spectrum of HIS-coupled DC-MNPs, it was noticed that HIS stretching vibrations of the carboxylate group appeared at 1607 and 1392 cm^{-1} , respectively, and the significant amino group stretching vibrations appeared at 3400 cm^{-1} [37]. The relevant peaks of dextran were introduced also without shifting [32, 35]. A new peak has arisen around 570 cm^{-1} that was assigned to the absorption of stretching vibration of Fe–O bond [22, 32, 35, 37].

3.3 Adsorption of control bacterial endotoxin on ligand-coupled MNPs and optimization of the experimental design

The removal of endotoxin from CBE solution was evaluated using the chromogenic kinetic method through the application of the previously mentioned equation to calculate the % removal. A fractional factorial design was employed using the following factors: ligand type, ligand concentration, CBE concentration, pH of incubation, temperature of incubation, and time of incubation. Two levels of each factor were chosen beside one center point to determine the optimum conditions for adsorption. Analysis of the fractional factorial design results was performed at 95% confidence level ($P < 0.05$) using the % removal as the response factor. A Pareto diagram was employed to introduce conclusions on the relative significance of the studied factors as well as the interactions between them, while the direction of effects was obtained from the normal plot of the standardized effects (Fig. 7). The only factor affecting the adsorption process was the ligand type as HIS showed that the best % removal result

was –85%. The optimized experimental conditions with the best %removal are demonstrated in Table 2.

3.4 Chromogenic kinetic assay

The bacterial endotoxin concentrations of the prepared CBE and spiked samples of peg-interferon and meningococcal polysaccharide were determined using a commercially available limulus amoebocyte lysate (LAL) kit according to the method described in European pharmacopeia monograph 2.6.14 method D [10]. The concentration of endotoxin in the samples was calculated using a standard curve. The coefficient of variation (CV) for the two replicates of both the sample and the positive product control (PPC) is less than 25%. Spike recovery of PPC within the range of 50–200% indicated no significant interference of the LAL reagent with the test sample, as per the FDA-approved kit specifications (ENDOSAFE®—PTS/MCS CARTRIDGES).

3.5 Kinetics of adsorption

The kinetic parameters are important to understand the adsorption mechanisms and rate-limiting step which are useful for designing and modeling commercial applications [38]. The adsorption capacity was calculated and plotted as previously mentioned (Fig. 8), and the kinetics study results are demonstrated in Table 3.

The correlation coefficients R^2 were used to describe the applicability of the adsorption kinetics models. The results showed that the adsorption kinetics of endotoxin on the ligand-coupled MNPs seems to obey the pseudo-second-order kinetic model ($R^2 = 0.9965$ and 0.9954) for HIS and PMB, respectively (Fig. 9), and the

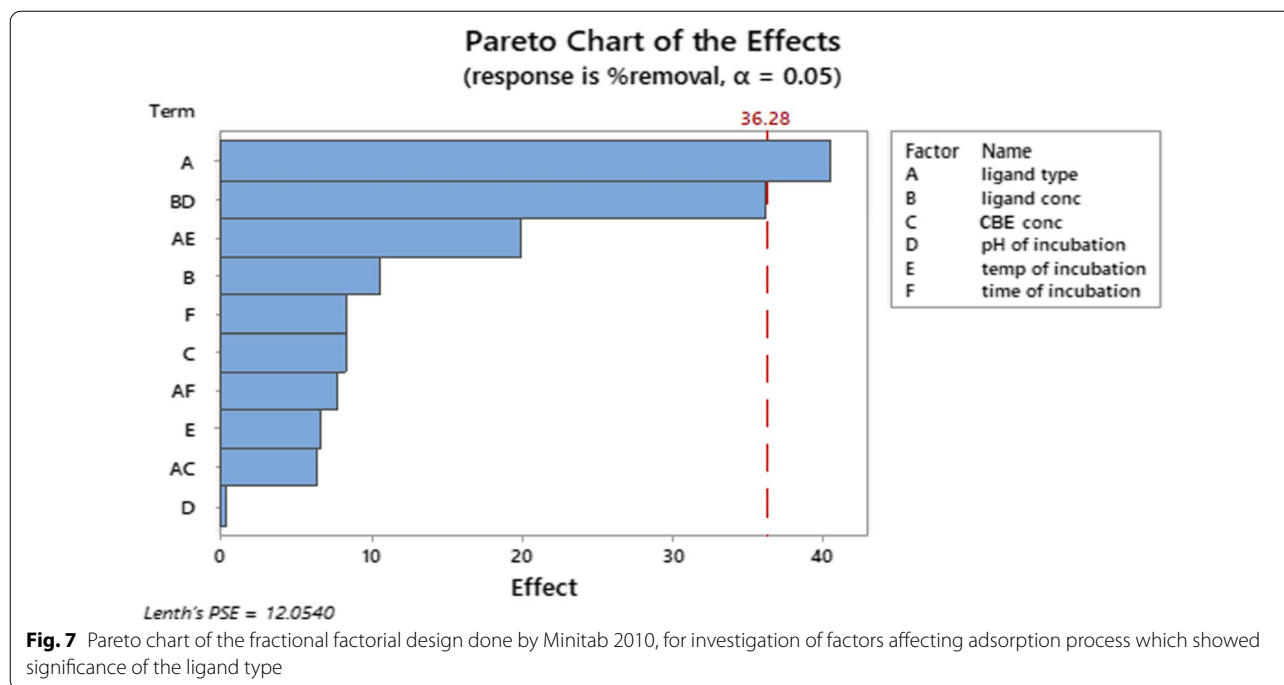


Table 2 Fractional factorial design for optimization of adsorption and results analysis

Ligand type	Ligand conc. ($\mu\text{g}/\text{ml}$)	CBE conc. (EU/ml)	pH of incubation	Temp of incubation ($^{\circ}\text{C}$)	Time of incubation (min)	%Removal
HIS	275	500,000	6.5	25	17.5	71.90
PMB	275	500,000	6.5	25	17.5	51.24
HIS	500	250,000	9	2-8	5	67.68
PMB	275	500,000	6.5	2-8	17.5	24.79
HIS	50	750,000	4	25	5	67.35
HIS	500	750,000	9	25	30	40.30
PMB	500	250,000	4	25	5	56.25
HIS	50	250,000	4	2-8	30	62.50
PMB	50	750,000	9	2-8	5	54.76
HIS	275	500,000	6.5	2-8	17.5	85.12
PMB	500	750,000	4	2-8	30	43.88
PMB	50	250,000	9	25	30	65.85

pseudo-second-order model seems to fit the data better than others as long as it had the most relatively complied value of Q_e calc in comparison with the Q_e expt. (Q_e calc = 0.2856 and 0.2166 mg/g for HIS and PMB, respectively). The R^2 values for the pseudo-first-order model (Additional file 1: Fig. S-4), intraparticle diffusion (Additional file 1: Fig. S-5), and Elovich (Additional file 1: Fig. S-6) models presented the lowest among the used models.

3.6 Adsorption isotherm

The results of experimental data obtained as demonstrated in Fig. 10 concluded that the adsorption isotherm data are fitting to Langmuir model with R^2 value 0.9997 and 0.9995 for histidine and PMB, respectively, compared to the results obtained by Freundlich model as demonstrated in Additional file 1: Fig S-8 with R^2 value 0.964 and 0.988 for histidine and PMB, respectively [33, 39].

The results also showed that endotoxin was removed at a maximum Langmuir adsorption capacity of 38.5 and 35.7 mg/g for histidine and PMB, respectively, as per Table 4.

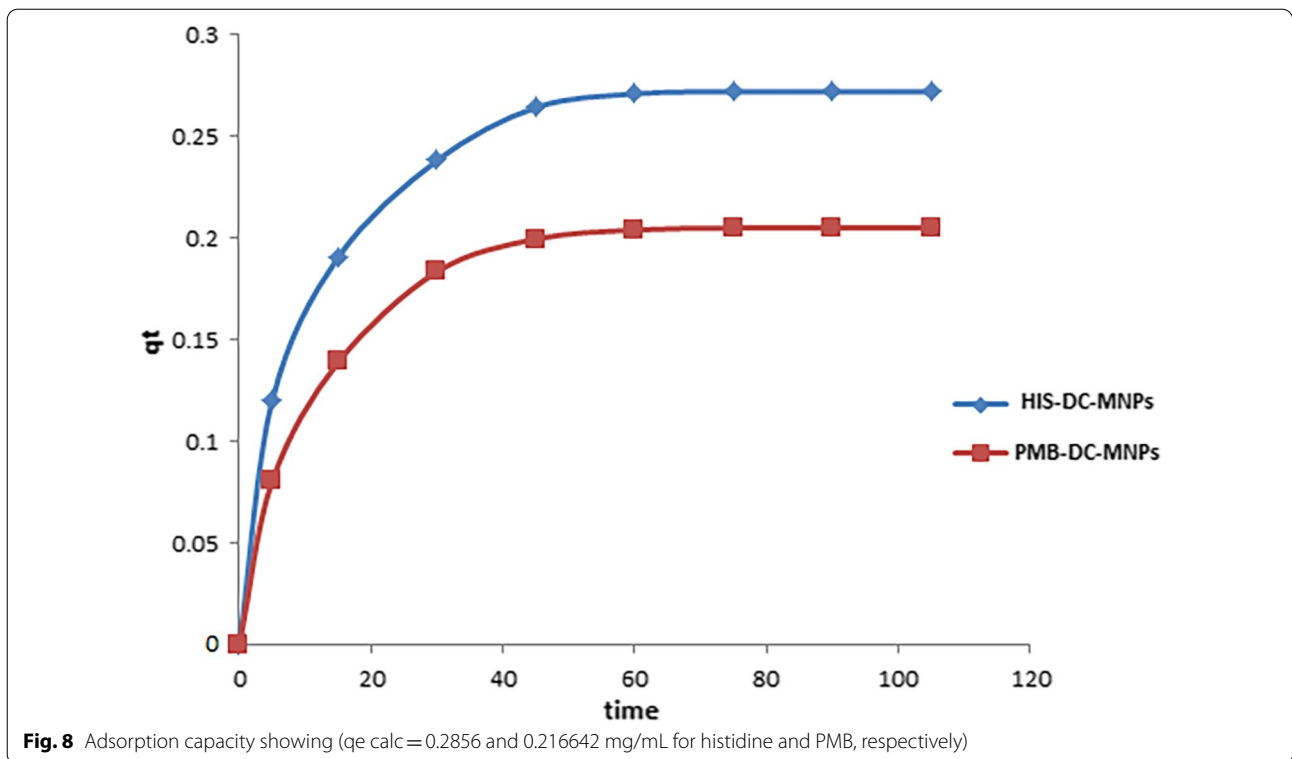


Table 3 Experimental kinetics models

	Pseudo-first order			
	$q_e \text{ expt}$	$q_e \text{ calc}$	k_1	R^2
HIS	0.272	0.046	0.379	0.967
PMB	0.205	0.050	0.437	0.959
	Pseudo-second order			
	$q_e \text{ expt}$	$q_e \text{ calc}$	k_2	R^2
HIS	0.272	0.285	0.063	0.996
PMB	0.205	0.216	0.043	0.995
	Elovich			
	$q_e \text{ expt}$	$q_e \text{ calc}$	β	R^2
HIS	0.272	0.060	0.017	0.972
PMB	0.205	0.046	0.008	0.972
	Intraparticle diffusion			
	$q_e \text{ expt}$	$q_e \text{ calc}$	k_{ip}	R^2
HIS	0.272	0.025	0.059	0.850
PMB	0.205	0.020	0.040	0.856

3.7 Application to incurred samples

The predetermined optimization conditions were applied in the purification of Peg-interferon and meningococcal polysaccharide vaccine by % removal of bacterial endotoxin $81.9 \pm 0.2\%$ and $82.6 \pm 0.15\%$,

respectively, which was followed by a second cycle of the experiment for complete removal of endotoxin from the tested biological samples. The tested samples were finished products spiked with 500,000 EU/ml CBE and incubated with 275 mg HIS-coupled MNPs

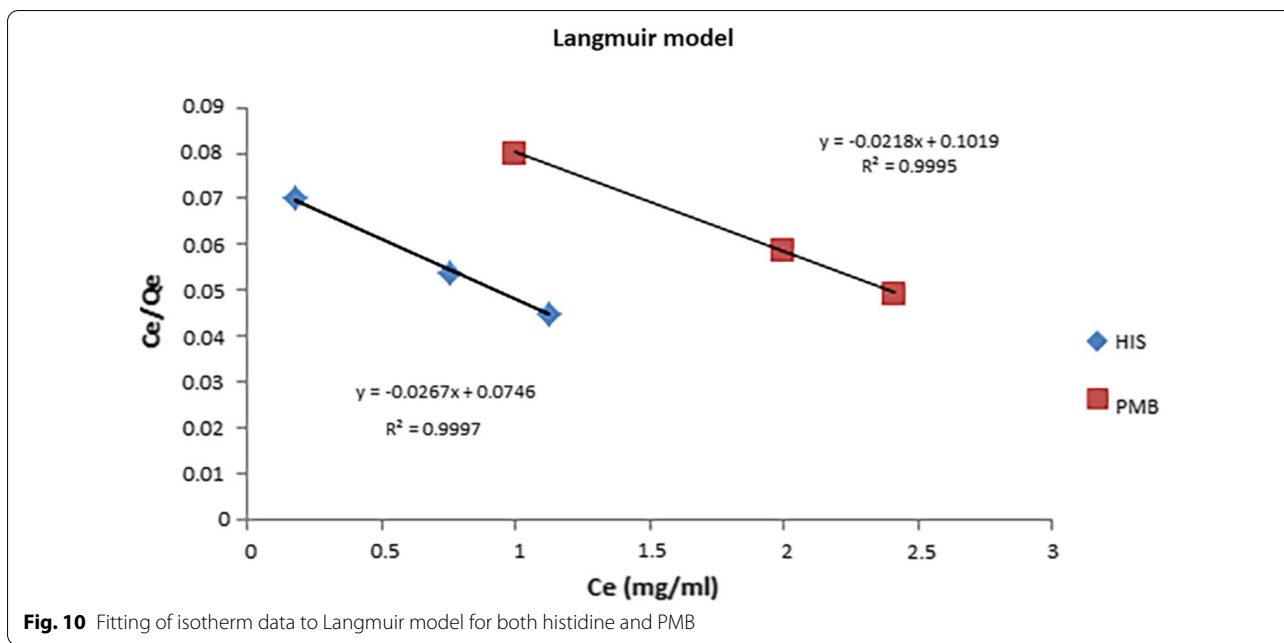
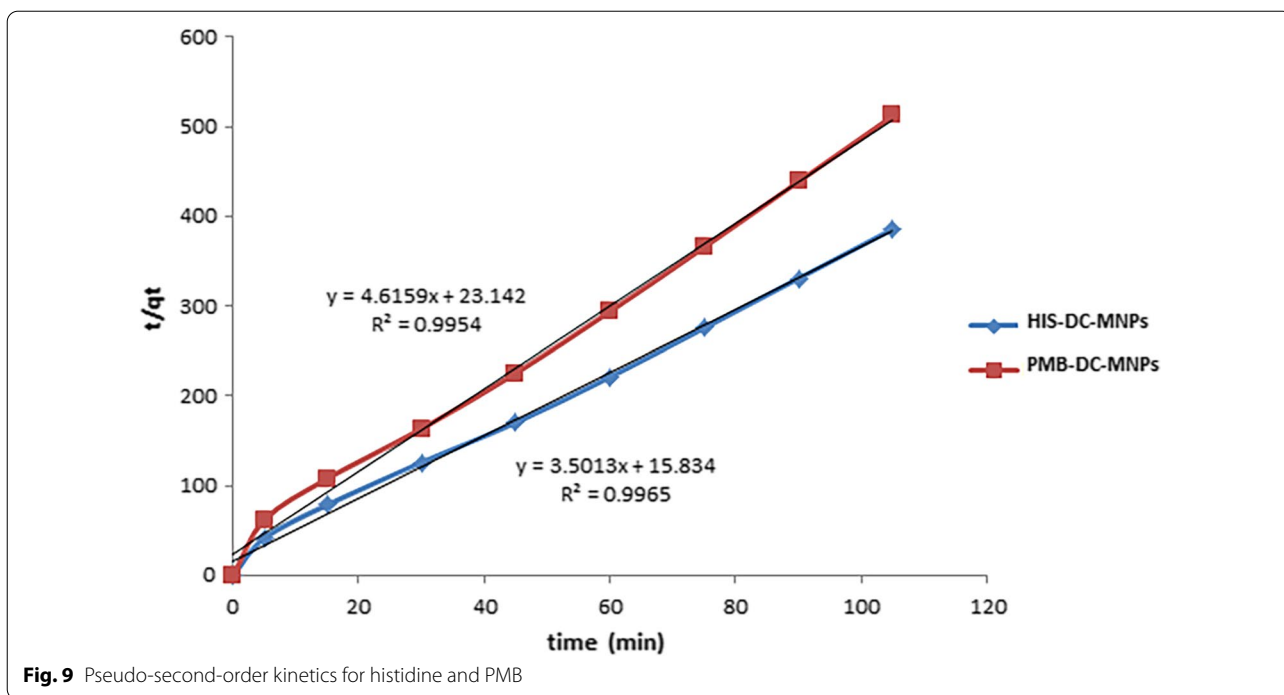


Table 4 Langmuir model isotherm

	HIS	PMB
R^2	0.9998	0.9995
Q_0	38.4615385	35.7142857
B	0.075	0.102

for 17.5 min at 2–8 °C with retained pH at 6.5. The endotoxin concentration was assessed by chromogenic kinetic assay before and after incubation with the HIS-coupled MNPs to calculate the % removal.

4 Discussion

Traditional methods of purification were previously employed to purify biologics from acquired endotoxin contamination [8, 9, 13–15]. Meanwhile, a lot of drawbacks were noticed as described before, including limited capacity and selectivity, expensive and complex procedures, and consumption of high time besides owing low yield.

In this study, the traditional drawbacks were overcome through the synthesis of magnetic nanoparticles as described above by a simple method and dextran was selected as a biocompatible coat as per its valuable characteristics over various types of coating materials. The developed magnetic nanoparticles were then coupled to either PMB or HIS and were challenged for their adsorption potential in purifying biologics from acquired endotoxin contamination as well as studying their adsorptive kinetics.

4.1 Preparation and optimization of dextran-coated MNPs

DLS is the most powerful analytical tool that can give direct hydrodynamic size information of the MNPs in addition to its unique feature in monitoring the colloidal stability of MNPs' suspension [40]. The PDI is a critical parameter for describing the degree of non-uniformity (heterogeneity) of the size distribution of these particles. Values of 0.4 and below are the most commonly acceptable results in practice for nanoparticle materials [41]. The significant effect on the particle size distribution (PDI) and solid content of the prepared MNPs may be explained as dextran protected MNPs from aggregation by providing repulsive electrostatic and/or steric interactions worked against the attractive van der Waals forces between MNPs [42]. As well, the results manifested that by adjusting the weight ratio of dextran to iron oxide to be more than 2.5, the diameter of nanoparticles decreased remarkably to be less than 50 nm and the solid content was enhanced. The reason behind this may be attributed as when the weight ratio of dextran to iron oxide is larger enough, more MNPs were modified by dextran, so the DC-MNPs are not easy to aggregate which in turn enhanced their stability and biocompatibility and promoted their suitability for biological applications [42]. The pH factor has a strong influence on the shape and mean size of MNPs components and also their size distribution. High pH motivates the MNPs to have a more spherical shape and more iron content besides a uniform size distribution with smaller size. The formation of MNPs looks like seed-mediated growth [43]. The temperature factor plays an important role in retaining the size distribution of MNPs with the same trend, which is assigned to the fact that the critical nucleus size was

larger at elevated temperature, and hence MNPs have a broader size distribution at the higher temperature [42, 44].

4.2 Characterization of the prepared MNPs

4.2.1 Transmission electron microscope (TEM)

It seems from the figures that increasing the concentration of the dextran coat to 50% w/v has caused the clustering of the MNPs within the matrix [22, 32]. Repulsive forces in between prevented the MNPs from sedimentation due to their well dispersion in the dextran matrix [32]. Figures 2, 3, and 4 demonstrate that the dark areas represented the iron oxide particles, while the lighter represented the polysaccharide structure [32]. The results complied with the previous results mentioned in the preliminary DLS screening in Sect. 3.1, and the literature regarding the dextran coating decreases the diameter of the resulted MNPs and prevents their agglomeration [22], the long-chain dextran polymer acts as surfactant coating to preserve an intermolecular space between the particles, thus maintaining their well dispersion [45].

4.2.2 X-ray diffraction (XRD)

The resulted diffraction peaks were reported to be characteristic for single-phase spinel structure of magnetite nanoparticles [32, 46].

The Scherrer's equation revealed an average particle diameter around 5.51 nm which was aligning with the results mentioned after the TEM analysis of the developed MNPs in part (3.2.1).

4.2.3 Magnetization measurements

The reported phenomenon was attributed to the high molecular weight of the dextran and the weight ratio of dextran to iron oxide in the MNPs [32]; as long as the density of the dextran shell increased, the magnetism was decreased [35].

4.2.4 Dynamic light scattering (DLS)

4.2.4.1 Zeta potential Zeta potential measurement evaluates the surface charge of nanoparticles and can be indicative of the extent of their stability [35]. The negative value of zeta potential for MNPs is due to the existence of OH⁻ groups on the surface of MNPs [32, 35]. The reduction in surface charge accompanied with dextran coating can be believed as the evidence of hydrogen bonding between the O⁻ groups of dextran with a hydroxyl group of MNPs [35].

4.2.4.2 Particle size distribution The result indicates that the effectiveness of dextran coating in shielding MNPs from aggregation consequently results in high dispersal capability of MNP with a uniform size distri-

bution [35]. The particle size obtained by DLS was larger than that obtained by TEM because the MNPs do not exist individually but aggregate with the entanglement of long chains of dextran [22, 47]. This result was aligned with the result obtained by TEM imaging that disclosed the role of dextran in protecting MNPs in their cluster form from agglomeration and revealed that the developed particles were retained in the nano-range even after being clustered [45].

4.2.5 Fourier transform infrared spectroscopy (FTIR)

The FTIR explanation has demonstrated that dextran was successfully coated on the surface of iron oxide particles through van der Waals force, hydrogen bond, and electrostatic interactions, which led to the effective coupling of PMB and HIS to the functionalized MNPs [22, 36, 37].

4.3 Adsorption of control bacterial endotoxin on ligand-coupled MNPs and optimization of the experimental design

Removal of endotoxin by both PMB- and HIS-coupled MNPs was accounted for synergistic hydrophobic and electrostatic interactions. Both ligands owned cationic and hydrophobic portions [2, 16]. PMB acts preferably in the pH range (6.0–10.0), and HIS acts in the pH range (4.0–9.0) [48]. Both ligands react successfully in solutions of ionic strength (μ) up to 0.5 after which dilution is required to retain the adsorption efficiency. HIS has exceeded PMB by overcoming its toxic effects upon accidental release from the removal system [8, 16].

4.4 Kinetics of adsorption

Pseudo-second-order kinetic model assumes that the chemisorption process may be the rate-limiting step in adsorption processes, which also depends on the availability of vacant binding sites on the adsorbent. It has been reported that the pseudo-first-order model fits better the adsorption in the early stage, but not the whole adsorption process [49]. Moreover, the nonlinearity of the intraparticle diffusion model indicates that the process is “complex” and multiple processes are limiting the overall adsorption rate [31].

It was reported that a bimolecular binding step is initiated relatively sterically unrestricted so that the amphipathic PMB molecule can be adopted in various orientations to bind the lamellar phase of BE. This is followed by a reorientation unimolecular step, most likely corresponding to a conformational change caused by the insertion of the hydrophobic portion of PMB

Table 5 Freundlich model isotherm

	HIS	PMB
R^2	0.9643	0.9878
Kf	2.48	1.64
1/n	0.18	0.35

into the nonpolar interior of the BE lamellar phase as shown in Additional file 1: Fig. S-7 [7].

Different peptides, mimic of PMB interactions, had a tendency for binding BE reasonably well, especially when owing asymmetric distribution of the hydrophobic and positively charged residues [7].

4.5 Adsorption isotherm

Langmuir isotherm model is based on the monolayer, homogeneous, and uniform energy on an adsorbent surface [39]. The previously mentioned results could be explained by uniform distribution of binding sites on the adsorbent NPs. Upon studying the Freundlich results, it can be clarified that 1/n values lied below one as per Table 5, which favors the chemisorption process assumption that was previously discussed in the adsorption kinetics.

5 Conclusions

Powerful magnetic nanoparticles were successfully synthesized using simple co-precipitation method and effectively coupled to PMB and HIS. Fractional factorial design was employed to optimize the preparation conditions and revealed that the significant factors were the concentration of the dextran solution and the combination between the pH and temperature of incubation. Fractional factorial design approach was also used to figure the applicability of endotoxin adsorption on the developed magnetic nanoparticles efficiently and to optimize the adsorption conditions as well. The adsorption kinetics was found to be fitting to pseudo-second-order model, and the adsorption isotherm study was found to be fitting to Langmuir model. The experimental study has introduced a new application for MNPs guiding the producers of biological products to improve their manufacturing process by granting a comprehensive, sensitive, and selective tool for purification of biologics from process-acquired endotoxin through the prepared ligand-coupled MNPs. It confirmed its ability on a pilot-scale application; meanwhile, future studies are needed to prove that the preparation is effective during the scale-up of the manufacturing process of biologics.

Supplementary Information

The online version contains supplementary material available at <https://doi.org/10.1186/s43088-022-00253-9>.

Additional file 1: Figure S-1. VSM chart for the prepared MNPs showing saturation magnetization (Ms) $1.2106 \times 10^{-3} \text{ emu g}^{-1}$. **Figure S-2.** FTIR chart of pure dextran-coated MNPs (a), pure PMB (b) and dextran-coated MNPs coupled to PMB (c), respectively; analysis was carried out in transmission mode following dispersion into KBr (potassium bromide). **Figure S-3.** FTIR chart of pure histidine (a), dextran-coated MNPs coupled to histidine (b), respectively; analysis was carried out in transmission mode following dispersion into KBr. **Figure S-4.** Pseudo-first-order kinetics for histidine and PMB. **Figure S-5.** Intraparticle diffusion model for histidine and PMB. **Figure S-6.** Elovich model for histidine and PMB. **Figure S-7.** Proposed model for binding of PMB to BE showing bimolecular binding step, in the first step PMB molecule binding to the lamellar phase of BE followed by a unimolecular step most likely corresponding to a conformational change caused by the insertion of the hydrophobic portion of PMB into the nonpolar interior of the BE lamellar phase. **Figure S-8.** Isotherm study by Freundlich model for both histidine and PMB.

Acknowledgements

Not applicable.

Author contributions

AS practical implementation of the study, result interpretation and data analysis. LH contributed to the manuscript writing and arrangements of the manuscript sections. FF reviewing the whole manuscript. MA designed the study, contributed to the supervision. MN supervised the study and contributed to the statistical analysis. All authors provided critical feedback and contributed to the final manuscript.

Funding

Not applicable.

Availability of data and materials

Not applicable.

Declarations

Ethics approval and consent to participate

Not applicable.

Consent for publication

Not applicable.

Competing interests

The authors have no conflicts of interest to declare that are relevant to the content of this article.

Author details

¹Egyptian Drug Authority, Cairo, Egypt. ²Analytical Chemistry Department, Faculty of Pharmacy, Cairo University, Cairo, Egypt. ³Bioanalysis Research Group, School of Pharmacy, Newgiza University, Giza, Egypt.

Received: 30 November 2021 Accepted: 10 May 2022

Published online: 18 May 2022

References

- Basauri A, Fallanza M, Giner-Robles L, Fernandez-Lopez R, Moncalián G, de la Cruz F, Ortiz I (2021) Integrated strategy for the separation of endotoxins from biofluids: LPS capture on newly synthesized protein. *Sep Purif Technol* 255:117689
- Petsch D, Anspach FB (2000) Endotoxin removal from protein solutions. *J Biotechnol* 76(2–3):97–119
- Pestka S (1983) The purification and manufacture of human interferons. *Sci Am* 249(2):36–43
- Joshi VS, Bajaj IB, Survase SA, Singhal RS, Kennedy JF (2009) Meningococcal polysaccharide vaccines: a review. *Carbohydr Polym* 75(4):553–565
- Basauri A, González-Fernández C, Fallanza M, Bringas E, Fernandez-Lopez R, Giner L, Moncalián G, de la Cruz F, Ortiz I (2020) Biochemical interactions between LPS and LPS-binding molecules. *Crit Rev Biotechnol* 20(3):292–305
- Gadre D, Carlson M, Mullan A, Kabundi I, Pedowitz N, Rieder SA, White N, Yu K, O'Connor E (2018) Endotoxin reduction in protein solutions using octyl β -D-1-thioglucoopyranoside wash on chromatography media. *J Chromatogr A* 1575:49–58
- Bhor VM, Thomas CJ, Suroliya N, Suroliya A (2005) Polymyxin B: an ode to an old antidote for endotoxic shock. *Mol Biosyst* 1(3):213–222
- Schneider M, Razdan S, Miller AM, Briceno ME, Barua S (2020) Current technologies to endotoxin detection and removal for biopharmaceutical purification. *Biotechnol Bioeng* 117(8):2588–2609
- Li Y, Boraschi D (2016) Endotoxin contamination: a key element in the interpretation of nanosafety studies. *Nanomedicine* 11(3):269–287
- Europe CO (2019) Bacterial endotoxin, European Pharmacopoeia Strasbourg:EDQM, European Directorate for the Quality of Medicines & HealthCare of the Council of Europe (EDQM): 209–213
- Gorbet MB, Sefton MV (2005) Endotoxin: the uninvited guest. *Biomaterials* 26(34):6811–6817
- Dullah EC, Ongkudon CM (2017) Current trends in endotoxin detection and analysis of endotoxin–protein interactions. *Crit Rev Biotechnol* 37(2):251–261
- Konwar A, Chowdhury D, Dan A (2019) Chitosan based in situ and ex situ magnetic iron oxide nanoparticles for rapid endotoxin removal from protein solutions. *Mater Chem Front* 3(4):716–725
- Ongkudon CM, Chew JH, Liu B, Danquah MK (2012) Chromatographic removal of endotoxins: a bioprocess engineer's perspective. *ISRN Chromatogr* 2012:1
- Mack L, Brill B, Delis N, Groner B (2014) Endotoxin depletion of recombinant protein preparations through their preferential binding to histidine tags. *Anal Biochem* 466:83–88
- Anspach FB (2001) Endotoxin removal by affinity sorbents. *J Biochem Biophys Methods* 49(1–3):665–681
- Salema V, Saxena L, Pattnaik P (2009) Removing endotoxin from biopharmaceutical solutions. *Pharm Technol Eur* 21(10):36
- Keçili R, Ghorbani-Bidkorbeh F, Dolak İ, Canpolat G, Karabörk M, Husain CM (2021) Functionalized magnetic nanoparticles as powerful sorbents and stationary phases for the extraction and chromatographic applications. *TrAC Trends Anal Chem* 143:116380
- Laurent S, Forge D, Port M, Roch A, Robic C, Vander Elst L, Muller RN (2008) Magnetic iron oxide nanoparticles: synthesis, stabilization, vectorization, physicochemical characterizations, and biological applications. *Chem Rev* 108(6):2064–2110
- Lu AH, Salabas EL, Schüth F (2007) Magnetic nanoparticles: synthesis, protection, functionalization, and application. *Angew Chem Int Ed* 46(8):1222–1244
- Bi F, Zhang J, Su Y, Tang YC, Liu JN (2009) Chemical conjugation of urokinase to magnetic nanoparticles for targeted thrombolysis. *Biomaterials* 30(28):5125–5130
- Hong R, Feng B, Chen L, Liu G, Li H, Zheng Y, Wei D (2008) Synthesis, characterization and MRI application of dextran-coated Fe₃O₄ magnetic nanoparticles. *Biochem Eng J* 42(3):290–300
- Jain TK, Richey J, Strand M, Leslie-Pelecky DL, Flask CA, Labhasetwar V (2008) Magnetic nanoparticles with dual functional properties: drug delivery and magnetic resonance imaging. *Biomaterials* 29(29):4012–4021
- Li J, Gao H (2008) A renewable potentiometric immunosensor based on Fe₃O₄ nanoparticles immobilized anti-IgG. *Electroanal Int J Devot Fundam Pract Asp Electroanal* 20(8):881–887
- Molday RS, MacKenzie D (1982) Immunospecific ferromagnetic iron-dextran reagents for the labeling and magnetic separation of cells. *J Immunol Methods* 52(3):353–367
- Pardoe H, Chua-Anusorn W, Pierre TGS, Dobson J (2001) Structural and magnetic properties of nanoscale iron oxide particles synthesized in the presence of dextran or polyvinyl alcohol. *J Magn Magn Mater* 225(1–2):41–46

27. Sahoo Y, Goodarzi A, Swihart MT, Ohulchanskyy TY, Kaur N, Furlani EP, Prasad PN (2005) Aqueous ferrofluid of magnetite nanoparticles: fluorescence labeling and magnetophoretic control. *J Phys Chem B* 109(9):3879–3885
28. Zhang J, Shao J, Guo P, Huang Y (2013) A simple and fast Fe₃O₄ magnetic nanoparticles-based dispersion solid phase extraction of Sudan dyes from food and water samples coupled with high-performance liquid chromatography. *Anal Methods* 5(10):2503–2510
29. Taitt CR, Shriver-Lake LC, Anderson GP, Ligler FS (2011) Surface modification and biomolecule immobilization on polymer spheres for biosensing applications. *Biomedical nanotechnology*. Springer, Berlin, pp 77–94
30. Ray SS, Gusain R, Kumar N (2020) Carbon nanomaterial-based adsorbents for water purification: fundamentals and applications. Elsevier, Amsterdam
31. Sahoo TR, Prelot B (2020) Adsorption processes for the removal of contaminants from wastewater: the perspective role of nanomaterials and nanotechnology. *Nanomaterials for the detection and removal of wastewater pollutants*. Elsevier, Amsterdam, pp 161–222
32. Attallah OA, Al-Ghobashy MA, Nebsen M, Salem MY (2016) Removal of cationic and anionic dyes from aqueous solution with magnetite/pectin and magnetite/silica/pectin hybrid nanocomposites: kinetic, isotherm and mechanism analysis. *RSC Adv* 6(14):11461–11480
33. Al-Ghouti MA, Da'ana DA (2020) Guidelines for the use and interpretation of adsorption isotherm models: a review. *J Hazard Mater* 393:122383
34. Li Z, Chen H, Bao H, Gao M (2004) One-pot reaction to synthesize water-soluble magnetite nanocrystals. *Chem Mater* 16(8):1391–1393
35. Khalkhali M, Sadighian S, Rostamizadeh K, Khoeini F, Naghibi M, Bayat N, Habibzadeh M, Hamidi M (2015) Synthesis and characterization of dextran coated magnetite nanoparticles for diagnostics and therapy. *Bioimpacts* 5(3):141–150
36. Lambadi PR, Sharma TK, Kumar P, Vasnani P, Thalluri SM, Bisht N, Pathania R, Navani NK (2015) Facile biofunctionalization of silver nanoparticles for enhanced antibacterial properties, endotoxin removal, and biofilm control. *Int J Nanomed* 10:2155–2171
37. Ünal B, Durmus Z, Baykal A, Sözeri H, Toprak M, Alpsoy L (2010) L-Histidine coated iron oxide nanoparticles: synthesis, structural and conductivity characterization. *J Alloy Compd* 505(1):172–178
38. Tapouk FA, Nabizadeh R, Nasseri S, Mesdaghinia A, Khorsandi H, Yousefi M, Alimohammadi M, Khoobi M (2020) Embedding of L-Arginine into graphene oxide (GO) for endotoxin removal from water: modeling and optimization approach. *Colloids Surf A* 607:125491
39. Tapouk FA, Nabizadeh R, Nasseri S, Mesdaghinia A, Khorsandi H, Mahvi AH, Gholibegloo E, Alimohammadi M, Khoobi M (2019) Endotoxin removal from aqueous solutions with dimethylamine-functionalized graphene oxide: modeling study and optimization of adsorption parameters. *J Hazard Mater* 368:163–177
40. Mahbubul I (2019) 3-Stability and dispersion characterization of nanofluid. Preparation, characterization, properties and application of nanofluid, micro and nano technologies. 47–112
41. Danaei M, Dehghankhold M, Ataei S, Hasanzadeh Davarani F, Javanmard R, Dokhani A, Khorasani S, Mozafari MR (2018) Impact of particle size and polydispersity index on the clinical applications of lipidic nanocarrier systems. *Pharmaceutics* 10(2):57
42. Lin Y, Zhang K, Zhang R, She Z, Tan R, Fan Y, Li X (2020) Magnetic nanoparticles applied in targeted therapy and magnetic resonance imaging: crucial preparation parameters, indispensable pre-treatments, updated research advancements and future perspectives. *J Mater Chem B* 8(28):5973–5991
43. Thanh NT, Maclean N, Mahiddine S (2014) Mechanisms of nucleation and growth of nanoparticles in solution. *Chem Rev* 114(15):7610–7630
44. Gyergyek S, Makovec D, Jagodič M, Drogenik M, Schenk K, Jordan O, Kovač J, Dražič G, Hofmann H (2017) Hydrothermal growth of iron oxide NPs with a uniform size distribution for magnetically induced hyperthermia: structural, colloidal and magnetic properties. *J Alloy Compd* 694:261–271
45. Abedini-Nassab R, Pouryosef Miandoab M, Şaşmaz M (2021) Microfluidic synthesis, control, and sensing of magnetic nanoparticles: a review. *Micromachines* 12(7):768
46. Abouzaid O, El Shawi OE, Mansour NA, Hanafy AM (2017) Synthesis and characterization of dextran coated magnetite nanoparticles loaded with curcumin and in vitro cytotoxicity study in MCF-7 cancer cells. *Benha Vet Med J* 33(2):365–374
47. Mudalige T, Qu H, Van Haute D, Ansar SM, Paredes A, Ingle T (2019) Characterization of nanomaterials: tools and challenges. *Nanomaterials for food applications*. Elsevier, Amsterdam, pp 313–353
48. Nawata M, Minobe S, Hase M, Watanabe T, Sato T, Tosa T (1992) Specific assay for endotoxin using immobilized histidine, limulus amoebocyte lysate and a chromogenic substrate. *J Chromatogr A* 597(1–2):415–424
49. Zhang Y, Yu F, Cheng W, Wang J, Ma J (2017) Adsorption equilibrium and kinetics of the removal of ammoniacal nitrogen by zeolite X/activated carbon composite synthesized from elutriite. *J Chem* 2017:1

Publisher's Note

Springer Nature remains neutral with regard to jurisdictional claims in published maps and institutional affiliations.

Submit your manuscript to a SpringerOpen[®] journal and benefit from:

- Convenient online submission
- Rigorous peer review
- Open access: articles freely available online
- High visibility within the field
- Retaining the copyright to your article

Submit your next manuscript at ► [springeropen.com](https://www.springeropen.com)
